Simulations in Nanobiotechnology

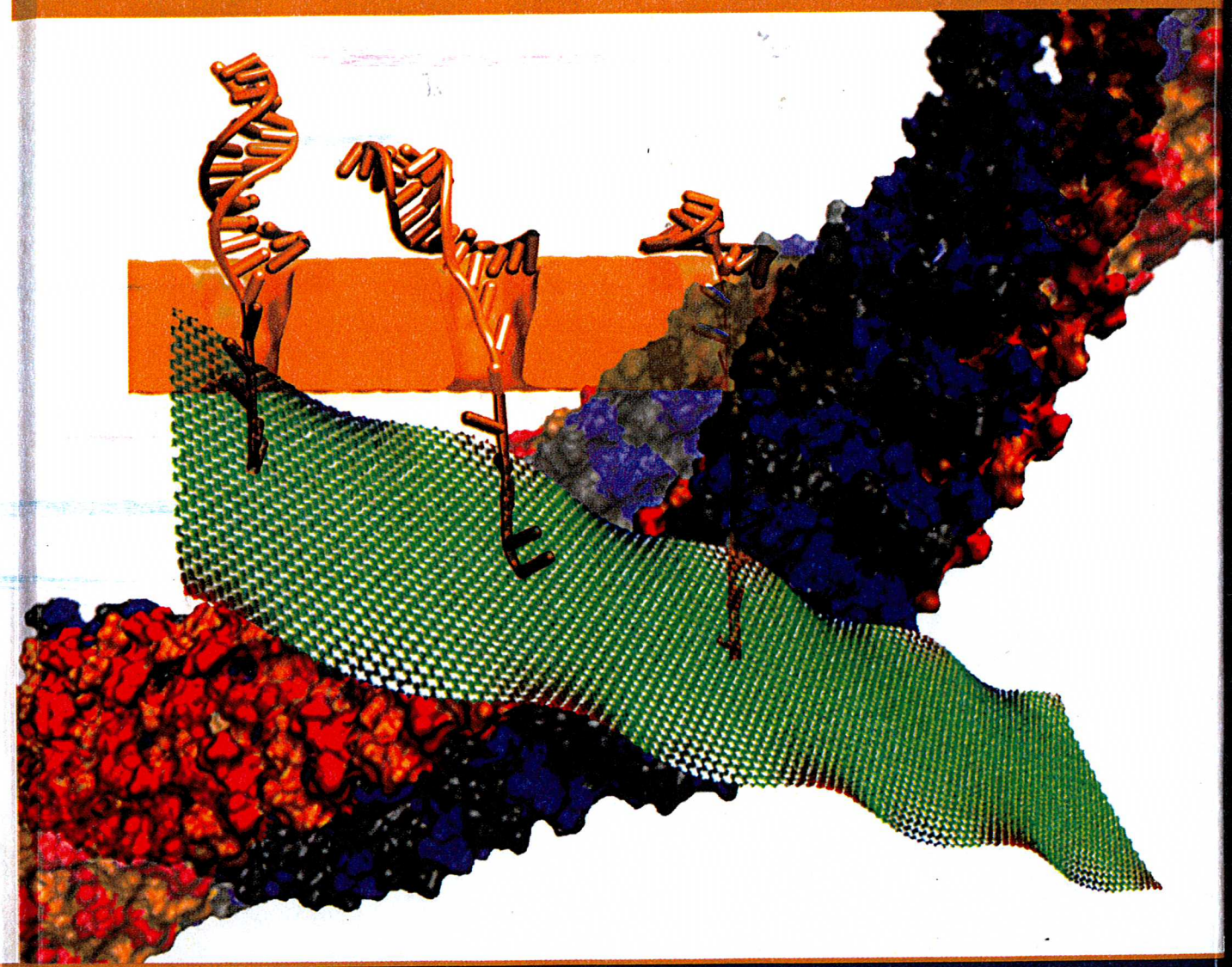

edited by Kilho Eom

CRC Press
Taylor & Francis Group

9 Resonant Theranostics
A New Nanobiotechnological Method for Cancer Treatment Using X-Ray Spectroscopy of Nanoparticles

Sultana N. Nahar, Anil K. Pradhan, and Maximiliano Montenegro

CONTENTS

9.1 INTRODUCTION

In biomedicine, cancer-related screening, diagnostic workup, image-guided biopsy and therapy delivery, and all X-ray sources such as simulators, linear accelerators, and computed tomography (CT) scanners generate broadband radiation. High-energy radiation doses are needed for sufficient tissue penetration, and higher exposure is needed for linear absorption. Hainfeld et al. (2004) found that irradiation with gold nanoparticles embedded in the malignant tumor is more effective than direct irradiation. Since X-rays interact more efficiently with high-Z elements, the nanoparticles are made of heavy high-Z elements that are *not* abundant in living tissues such as C, O, and Fe. They are also chosen to be nontoxic after injecting into the body and designed with antigens that seek out antibodies produced in the tumor. Some of the high-Z elements in medical applications are bromine, iodine, gadolinium, platinum, and gold, which are used in compounds that do not react unfavorably in the body. High-energy irradiating X-rays interact mainly with heavy elements, while lighter elements remain inactive because of low absorptivity. The typical size of a nanoparticle varies from a few nanometers to a few tens of nanometers and hence can penetrate vascular cells of typical sizes <30 nm or so. The high-energy X-rays have an additional advantage that they can penetrate the tissue before much loss of energy and reach the embedded nanoparticles.

Among the radiosensitizing agents commonly used in medicine are bromodeoxyuridine (BUdR) or iododeoxyuridine (IUdR) that contain atoms of moderately heavy elements. Increasingly, the application of nanobiotechnology entails nanoparticles made of high-Z elements such as platinum and gold. Although the background X-ray absorption cross sections are large for ionization of outer electron shells, they are small for inner-shell electrons. But the inner-shell electrons are more likely to be ionized at high X-ray energies needed for deep penetration into the body tissue.

Gold nanoparticles have been extensively taken into account in nanobiotechnology applications, especially for in vivo cancer treatment because of their interaction with high-energy X-rays and nontoxicity. Laboratory experiments, using gold nanoparticles injected into mice tumors and then irradiated with high-energy 140–250 keV X-rays, have shown considerable reduction in tumor sizes (Hainfeld et al. 2004). The K-shell ionization energy of gold is 80.73 keV. Therefore, a 250-kVp X-ray source with output energies up to 250 keV is capable of ionizing all inner n-shells and subshells of the gold atom, with L-, M-, N-, O-, P-shell ionizations approximately at 12–14, 3.4–2.2, 0.11–0.9, 0.01–0.11, 0.0.009 keV, respectively.

In an effort to narrow down the radiation bandwidth, and to enable sufficient penetration, our earlier investigations (Pradhan et al. 2009; Montenegro et al. 2009) have focused on K-shell ionization of heavy elements (Nahar, Pradhan, and Sur 2008). Sharp edges in photoionization cross sections at threshold energies of various electronic shells are well known. Hence, energies at the K-shell ionization, or somewhat above, are expected to initiate enhanced emission of electrons and photons through the Auger process. However, this enhancement has not been achieved (Larson et al. 1989). We discuss the reason for this in Section 9.2 and describe a method that targets the energy bands in which such *resonant* enhancements are possible.

9.2 RESONANT THERANOSTICS

We have investigated a novel approach "resonant theranostics" (RT) (Pradhan et al. 2007; Silver, Pradhan, and Yu 2008; Pradhan et al. 2009; Montenegro et al. 2009) for more precise radiation therapies and diagnostics with reduced harmful exposure. RT proposes the use of a monochromatic X-ray source to irradiate heavy-element (high-Z) nanoparticles as shown in Figure 9.1. Tumors could be doped with these nanoparticles of heavy elements. The irradiating X-rays will be focused at resonant frequencies on the nanoparticles. We will illustrate that there are resonant energies at which X-ray absorption probability increases by orders of magnitude. Through accurate atomic calculations, we can determine these energy ranges and the strength of these resonances (e.g., for platinum and uranium, see Nahar, Pradhan, and Lim 2011). Hence, the incident X-rays need to be not only monochromatic but also preselected for maximum interaction cross sections.

Use of narrow-band resonant energies in diagnostics spectroscopy can provide more detailed microscopic and accurate information in contrast to broadband imaging. Also, spectroscopically targeted radiation should be far more efficient with reduced exposure. In Section 9.2.1, we discuss some basics of producing the monochromatic X-rays. Focusing the impinging X-rays to resonant energies will require more elaborate details to understand the physical processes, and these will be discussed in Section 9.4. Numerical simulations are then performed to see the effect of the atomic/molecular/biological processes in the body tissue along potential pathways.

9.2.1 Production of Monochromatic X-Rays

In a typical X-ray machine, a beam of electrons is accelerated across the potential difference between the cathode and the anode and strikes a high-Z target such as tungsten, producing Bremsstrahlung radiation at all energies from zero to the peak value of the potential. The typical shape of the emitted Bremsstrahlung spectrum

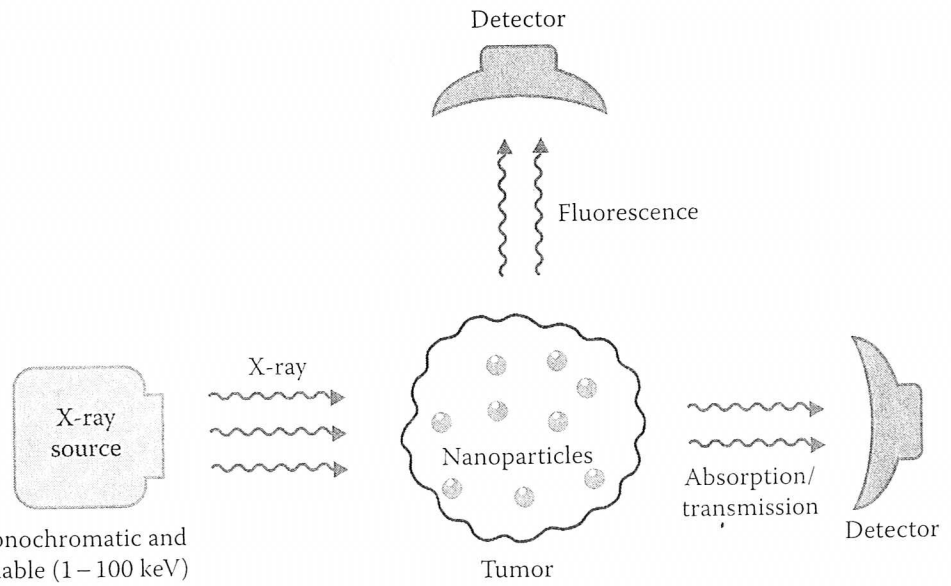

FIGURE 9.1 Schematic diagram of resonant theranostics.

shows a maximum around one-third of the output peak voltage (expressed as kVp or MVp). For example, a conventional high-energy linear accelerator (LINAC) with a peak voltage of 6 MVp produces radiation up to 6 MeV, but with a broad maximum around 2 MeV. Although there are a number of accelerator facilities around the world to produce X-rays via synchrotron radiation, they are expensive and impractical for common usage.

One of the main ideas of RT is to produce monochromatic X-rays using generally available X-ray machines. Bremsstrahlung radiation from a conventional X-ray source may be directed toward a high-Z target, rotated at a selected angle. Inner-shell ionizations, followed by radiative decays from outer shells, would produce X-ray fluorescence at monochromatic energies. For instance, the intensity of the monochromatic K_α radiation from partial conversion of Bremsstrahlung radiation that causes K-shell ionizations can be estimated as follows:

$$I(K_\alpha) \sim N(X) \int_{E \geq E_k}^{E(\mathrm{kVp})} f_\mathrm{B} \sigma_\mathrm{K}(E)\, \mathrm{d}E$$

where $N(X)$ is number density of atoms of element X, f_B is the Bremsstrahlung flux distribution in energy, and σ_K is the K-shell photoionization cross section. It may be assumed to a good approximation that each K-shell ionization leads to the ejection of a K_α photon. The K-fluorescence yield ω_K may be obtained from the branching ratio as

$$\omega_K = A_\mathrm{r}(L-K)/[A_\mathrm{r}(L-K) + A_\mathrm{a}(L)]$$

where $A_\mathrm{r}(L-K)$ is the radiative decay rate from L to K shell and A_a is the autoionization decay rate, respectively. For high-Z elements such as platinum and uranium, the K-fluorescence yield ($\omega_K > 0.95$) approaches unity. Hence, all photons from the Bremsstrahlung source above the K-shell ionization energy, $E > E_K$, may be *converted* into monochromatic K_α radiation with high efficiency. Then, monochromatic deposition of X-ray energy may also be localized using high-Z nanoparticles. The RT scheme predicts considerable production of electron ejections and photon emissions via the Auger process and secondary Coster–Kronig and super-Coster–Kronig branching transitions (the relevant atomic physics is described in the textbook "Atomic Astrophysics and Spectroscopy," Pradhan and Nahar [2011]).

9.3 X-RAY INTERACTION WITH NANOPARTICLES

X-ray interaction with high-Z atoms implies inner-shell ionization, absorption, and emission via Auger processes. Although high-Z elements are now commonly used in nanobiotechnology, their detailed physical properties are relatively unknown either experimentally or theoretically. To establish the conceptual framework of the RT technology, it is important to understand the precise interaction of X-rays as a function of incident energy and the atomic structure of the target. We illustrate that resonances are formed during X-ray–nanoparticle interaction at energies *below* the K-shell ionization energy and that these resonances represent the enhancement of absorption coefficients by orders of magnitude.

9.3.1 Radiative Processes of Photoabsorption, Photoemission, and Opacity

Interaction between an atomic species X^{+Z} of charge Z and an X-ray photon ($h\nu$) can involve the following processes.

Photoexcitation: An electron in an atomic or a molecular system, X^{+Z}, absorbs the photon and jumps to a higher excited level while remaining in the atomic or molecular system:

$$X^{+Z} + h\nu \rightarrow X^{+Z*}$$

The asterisk (*) denotes an excited state. The oscillator strength (f) represents the strength of the transition. Deexcitation (inverse of excitation) occurs as an excited electron drops down to a lower state, typically to the ground state by emitting a photon. The atomic parameter for this process is the radiative decay rate or the Einstein A-coefficient.

Photoionization/photodissociation/photoelectric effect: An electron absorbs a photon and leaves the atom or molecule:

$$X^{+Z} + h\nu \rightarrow X^{+Z+1} + e$$

This direct process gives the *background* photoionization. It can also occur via an intermediate doubly excited autoionizing state, leading to autoionization (AI) when the electron goes free, or to dielectronic recombination (DR) when a photon is emitted with capture of the interacting electron, that is,

$$X^{+Z+1} + e \leftarrow\rightarrow (X^{+Z**}) \leftarrow\rightarrow (X^{+Z} + h\nu)\ (DR)$$

or

$$\leftarrow\rightarrow X^{+Z+1} + e\ (AI)$$

For photoionization, we calculate cross section σ_{PI}. The intermediate doubly excited state (double asterisks), in which two electrons are in excited levels, manifests itself in a resonance in the cross section.

Collision excitation: An atom or a molecule goes to an excited state by the impact of a free electron and later decays by emitting a photon.

$$X^{+Z} + e \rightarrow X^{+Z*} + e'$$

This collision process can also occur through an intermediate doubly excited autoionizing state, that is, a resonance. The atomic parameters for the process are the collision strength and the collision cross section.

9.3.2 Auger Process and Coster–Kronig Cascades

Photoionization through ejection of an inner-shell electron creates a hole in the electronic structure of an atomic system and leads to the Auger effect. The Auger effect is a

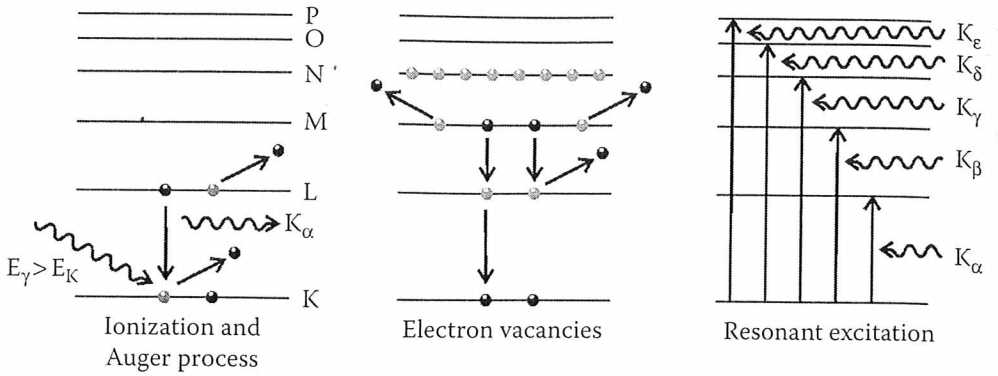

FIGURE 9.2 Schematic diagrams of (a) Auger process, (b) Coster–Kronig cascades, and (c) resonant photoexcitation. (From Pradhan, A. K., S. N. Nahar, M. Montenegro, Y. Yu, H. L. Hang, C. Sur, M. Mrozik, and R. M. Pitzer. 2009. *J Phys Chem A* 113:12356–63. With permission.)

downward transition of an upper level electron to the lower inner-shell hole when the transition energy is released as a photon.

The Auger process and related cascades are illustrated in Figure 9.2. Figure 9.2a shows a 1*s* electron in the *K*-shell ejected by absorption of an X-ray photon of energy higher than the *K*-shell ionization energy, $E_\gamma > E_K$, creating a hole or vacancy. An *L*-shell electron drops down filling the hole, and the transition energy between the *K*-shell and the *L*-shell is released as a photon. Figure 9.2b illustrates the Coster–Kronig cascade effect, which causes ejection of more electrons. The emitted photon in the Auger process may knock out another *L*-shell electron, resulting in two holes in the *L*-shell. The holes may then be filled up by the decay of two electrons of the higher level, say from the *M*-shell, along with emissions of two photons. Hence with each decay the number of holes, and thereby the emitted electrons and photons, may double. This cascading process, known as the Coster–Kronig process, will continue until the vacancies reach the outermost level. This can result in up to 20 or more electrons released in a single *K*-shell ionization of a high-*Z* atom with electrons up to *O* and *P* shells, such as in gold. Most of these electrons are at low energies since they are ejected from high-lying outer shells. The *reverse* process of resonant photoexcitation (Figure 9.2c) is discussed in Subsection 9.4.2.

9.4 PARAMETERS FOR ATOMIC PROCESSES

The parameters for these atomic processes can be obtained from atomic structure calculations (e.g., Nahar, Pradhan, and Sur 2008), or from the more elaborate R-matrix method (e.g., Nahar et al. 2003). The wave function, ψ_B for the bound state and ψ_F for the continuum or free state, and energies can be obtained by solving the Schrodinger equation:

$$H\psi = E\psi$$

We employ the relativistic Breit-Pauli (BP) approximation to calculate the parameters. The BP Hamiltonian H_{BP} is written as

$$H_{\mathrm{BP}} = H_{\mathrm{NR}} + H_{\mathrm{mass}} + H_{\mathrm{Dar}} + H_{\mathrm{so}} + \frac{1}{2}\sum_{i\neq j}^{N}[g_{ij}(\mathrm{so}+\mathrm{so}') + g_{ij}(\mathrm{ss}') + g_{ij}(\mathrm{css}') + g_{ij}(\mathrm{d}) + g_{ij}(\mathrm{oo}')]$$

where the nonrelativistic Hamiltonian is

$$H_{\mathrm{NR}} = \sum_i \left[\nabla^2 - \frac{2Z}{r_i} + \sum_{j>i}\frac{2}{r_{ij}}\right]$$

The one-body correction terms are

$$H_{\mathrm{mass}} = -\frac{\alpha^2}{4}\sum_i p_i^4, \quad H_{\mathrm{Dar}} = -\frac{\alpha^2}{4}\sum_i \nabla^2\left(\frac{Z}{r_i}\right), \quad H_{\mathrm{so}} = \alpha^2\sum_i \frac{Z}{r_i^3} l_i \cdot s_i$$

where l_i and s_i are orbital angular momentum and spin angular momentum of individual electrons. The rest are two-body correction terms. Of them, the most important part is the Breit interaction term.

$$H_{\mathrm{B}} = \frac{1}{2}\sum_{i\neq j}^{N}[g_{ij}(\mathrm{so}+\mathrm{so}') + g_{ij}(\mathrm{ss}')]$$

In these equations, s stands for spin, s′ for other spin, o for orbit, o′ for other orbit, c for contraction, and d for Darwin. In the present calculations, terms up to the Breit interaction are included. The last three weak terms are neglected. In the Breit interaction term

$$g_{ij}(\mathrm{so}+\mathrm{so}') = -\alpha^2\left[\left(\frac{r_{ij}}{r_{ij}^3}\times p_i\right)\cdot(s_i + 2s_j) + \left(\frac{r_{ij}}{r_{ij}^3}\times p_j\right)\cdot(s_j + 2s_i)\right]$$

$$g(\mathrm{ss}') = 2\alpha^2\left[\frac{s_i s_j}{r_{ij}^3} - 3\frac{(s_i r_{ij})(s_j r_{ij})}{r_{ij}^5}\right]$$

Substitution of wave function expansion, which is a linear combination of configuration state functions, in the Schrodinger equation yields bound states ψ_{B} when $E < 0$, and free or continuum states ψ_{F} when $E > 0$. More details of the theory can be found in the study by Nahar (2006) and the study by Pradhan and Nahar (2011).

Due to electromagnetic interaction, the bound–bound transition matrix is given by $\langle\psi_{\mathrm{B}}\|D\|\psi_{\mathrm{B}'}\rangle$, where $D = \Sigma_i(r_i)$ is the dipole operator of the atomic system of N-electrons (the $\|$ notation represents a reduced matrix element). For the bound-free photoionization, the transition matrix is $\langle\psi_{\mathrm{F}}\|D\|\psi_{\mathrm{B}}\rangle$. These matrix elements can be reduced to give the desired quantity the line strength S as follows:,

$$S = \left|\langle\psi_f\left|\sum_{j=1}^{N} r_j\right|\psi_i\rangle\right|^2$$

The oscillator strength f_{ij} and radiative decay rate A_{ji} for the bound–bound transition can be obtained from the line strength as

$$f_{ij} = [E_{ji}/(3g_i)]S,\ A_{ji}(s^{-1}) = [0.8032 \times 10^{10} E_{ji}^{3}/(3g_j)]S$$

where g_i and g_j are statistical weight factors of states i and j, respectively. The photoionization cross section for bound-free transitions can be obtained from the corresponding line strength as follows:

$$\sigma_{PI}(\nu) = [4\pi^2 \alpha a_o^2 E(Ry)]/(3g_i)S$$

where α is the fine structure constant, a_o is the Bohr radius in centimeters, E is the photon energy in Ry, and g_i is the statistical weight factor of the initial ion.

We may refer to the resonant transitions to doubly excited states above the ionization threshold as "Auger line strengths." The K-shell transitions ($1s$-np), such as K_α, K_β, K_γ, with $n = 2, 3, 4, \ldots$, are examples of these resonant transitions. They appear at energies of corresponding transitions; their cross sections can be obtained from their Auger line strengths and using the above equation for σ_{PI}.

The other useful quantity for propagation of radiation in a medium is the mass absorption or attenuation coefficient κ. Since κ is related to σ_{PI}, it may be expressed in terms of units of mass as follows:

$$\kappa(\nu) = \sigma_{PI}/(uW_A)$$

where u is atomic mass unit, amu = 1.66054e-24 g, and W_A is the atomic weight of the element being photoionized. It is also the same quantity as the plasma opacity for interaction cross section per density, cm^2/g.

The κ derived from oscillator strengths correspond to a single-line resonance. However, a resonance in a medium has a structure spread over an energy width. Broadened resonant structures of various K-shell transitions in photoionization cross sections can be obtained from Auger line strengths by convolving the resonant cross sections over a normalized Gaussian function $\varphi(\upsilon)$ as (e.g., Seaton et al. 1994)

$$\sigma_{PI}(\nu)\ \varphi(\upsilon) \quad \text{where } \int \varphi(\upsilon)d\nu = 1$$

$\varphi(\upsilon)$ can be a Gaussian function of form

$$\varphi(E = h\upsilon) = [1/\sqrt{(2\pi)}]\ \Delta E \exp[-E^2/(2\Delta E^2)]$$

where ΔE is the width of the resonant profile.

9.4.1 Transmitted Intensity of X-Rays

The attenuation of radiation through a plasma depends on temperature, density, and the component material. Quantitatively the radiation intensity decreases exponentially and can be described as (NIST)

$$I(\nu) = I_0(\nu)\exp[-(\sigma/\rho)x] = I_0(\nu)\exp[-\kappa(\nu)x]$$

where I_0 is the incident intensity, σ is the photoionization cross section, ρ is the density of the plasma, and x is the depth.

9.4.2 Incident Flux for Resonant Absorption

With vacancies in the L-shell, it is possible to have the inverse of the Auger decay, that is, a K-shell electron may be excited upward to fill up the L-shell hole under an external photon field, as illustrated in Figure 9.2c. A photon can induce the K-electron to go through the resonant K_α transition and create a hole in the K-shell. Such a condition will present a competition between the downward decay and the upward excitation. The process can be represented as the Einstein A-coefficient for radiative decay and the B-coefficient for photon absorption (e.g., Pradhan and Nahar 2011)

$$A_{ji}(\nu) + B_{ji}(\nu)\,\rho_{ij}(\nu) = B_{ij}(\nu)\,\rho_{ij}(\nu)$$

for any two-level system $i \rightarrow j$, transition frequency ν, and radiation field density $\rho_{ij}(\nu)$. In the special case of no downward transitions into the K-shell, because it may be filled, there will be no stimulated emission. For such a situation, we can rewrite the B and A coefficients including only radiative transitions from higher n-shells to fill the L-shell vacancy, also competing with upward K-shell excitations. Given the incident photon flux Φ at the resonant energy of K_α, we can write (Pradhan et al. 2009)

$$\Phi(K_\alpha)g_K B(K_\alpha) = \sum_{n_i>2} g_i A[n_i(S_i L_i J_i) \rightarrow 2(SLJ)]$$

where $n_i(S_i L_i J_i)$ refers to specific fine structure levels of an n-shell, for example, $2(S_i L_i J_i)$ refers to the L-shell levels, and g_K and g_i are the statistical weights of the K-shell and excited levels i, respectively. The above condition suggests a *critical photon density* Φ_c could be defined such that any flux greater than

$$\Phi_c(K_\alpha) = \left\{\sum_{n_i>2} g_i A\left[n_i(S_i L_i J_i) \rightarrow 2(SLJ)\right]\right\} / g_K B(K_\alpha)$$

could initiate the resonant absorption for upward excitation to fill an L-shell hole.

The radiative decay coefficients for a high-Z element, such as gold and platinum are very large (Nahar, Pradhan, and Sur 2008; Nahar, Pradhan, and Lim 2010), and any vacancy in the L-shell is likely to be filled on a relatively short timescale by a radiative transition from a higher shell, given transition array coefficients $A(M \rightarrow L)$ of approximately 10^{14-15} s^{-1} and $A(L \rightarrow K)$ of approximately 10^{15-16} s^{-1}. Since the resonant absorption $B(K_\alpha)$ coefficients are related to the $A(K_\alpha)$ coefficients by the factor $[c^3/(8\pi h\nu^3)]$ (e.g., Pradhan and Nahar 2011), we find that for high-energy X-ray transitions, the $B(K_\alpha)$ are of the same order of magnitude as the $A(M \rightarrow L)$. Therefore, the RT mechanism also invokes the fact that X-ray irradiation of high-Z atoms results in Auger decays of photon emission and electron ejections creating multiple

electron vacancies. These vacancies may be filled either by radiative decays from higher electronic shells or by excitations from the K-shell at resonant energies by an external X-ray source. Calculations of $\Phi_c(K_\alpha)$ require a large number of A and B coefficients, photon fluency rates, and photoabsorption cross sections for high-Z atoms to be computed, as described in Section 9.5.

9.5 X-RAY-INDUCED RADIATIVE TRANSITION RATES AND CROSS SECTIONS IN BROMINE AND GOLD

We aim at studying the physical processes due to irradiation of X-rays at resonant energies by high-Z material embedded in the body tissue. The radiosensitizing agents commonly used in medicine are BUdR or IUdR that contain heavy elements bromine and iodine, respectively. For BUdR, irradiating high-energy X-rays will interact mainly with bromine ($Z = 35$), while remaining transparent to lighter elements H, N, O. The incident energy should be more than the K-shell ionization energy of 13.5 keV of bromine because lighter elements have K-shell ionization energies $E < 0.5$ keV and the photoionization cross sections decrease as E^{-3}.

Let a neutral bromine atom with ground configuration $1s^2 2s^2 2p^6 3s^2 3p^6 3d^{10} 4s^2 4p^5$ undergo L-shell ionization by an external X-ray source, with the residual configuration with a $2p$-hole: $1s^2 2s^2 \mathbf{2p^5} 3s^2 3p^6 3d^{10} 4s^2 4p^5$. This state lies above the bound state energies and is a short-lived autoionizing one that decays quickly. As explained earlier, such decay may introduce a resonance in the absorption or ionization cross section. The external radiation can induce a ($1s$-$2p$) transition such that a K-shell electron absorbs an X-ray photon and jumps into the L-shell hole. In the inverse situation, bromine is ionized through a K-shell electron, and an L-shell electron may decay down to the K-shell, with emission of a photon. The line strength for the $1s$-$2p$ transition is the same for both the processes. But other quantities such as oscillator strength and the radiative decay rate can differ because of their dependence on kinematical factors and energy.

The resonances due to $1s$-np (where $n = 2, 3, 4, \ldots$) transitions lie below the $1s$ or K-shell ionization energy. Table 9.1 presents oscillator strengths and corresponding cross sections and photoabsorption coefficients for $1s$-$2p$, $1s$-$3p$, and $1s$-$4p$ transitions for the singly ionized bromine, bromine II (Nahar et al. 2010). For atomic or molecular ions, many transitions are possible if electron vacancies exist in subshells, thereby allowing for strong dipole upward excitation transitions by incident photons. Radiative attenuation coefficients, or plasma opacities, are greatly enhanced due to such resonant line transitions, which will be illustrated in Section 9.6. Because of the formation of various states with the same configuration, the number of transitions could be large. For example, there are 30 different transitions among states arising from configurations of $2p^5$ and $1s$ while the rest of the orbital occupations remain the same in bromine II. Table 9.1 lists all 30 transitions for $1s$-$2p$ transitions, while only the total transition parameters are given for $1s$-$3p$ and $1s$-$4p$ transitions. The table shows the decrease in total f, cross section (CS), and absorption coefficient κ as n increases. These transition parameters were computed through configuration interaction calculations in the relativistic BP approximation using the atomic structure code SUPERSTRUCTURE (SS) (Eissner, Jones, and Nussbaumer 1974, Nahar et al. 2003) and PRCSS (e.g., Nahar 2006).

TABLE 9.1

Transition Parameters f_{ij}, S, A_{ji}, Cross Section σ_{PI}, and Absorption Coefficient κ for Resonant 1s-2p, 1s-3p, and 1s-4p Transitions in Unfilled *np* Subshells of Bromine II (Ground: $1s^2 2s^2 2p^6 3s^2 3p^6 3d^{10} 4s^2 4p^4$). LS Multiplets Are from the Same Spin-Multiplicity Transitions

Z	Ne	slpc:i	slpc:j	g_i	g_j	wl (Å)	E (keV)	E_i (Ry)	E_j (Ry)	f_{ij}	S	A_{ji} (s − 1)	σ_{PI} (Mb)
							$C_i(9)=1s^2 2s^2 2p^5 \ldots 4p^5$, $C_j(11)=1s 2s^2 2p^6 \ldots 4p^5$						
35	34	3Se 9	3Po11	3	5	1.033	12.002	118.37	1000.86	1.66E−02	1.69E−04	6.24E+13	1.34E−01
35	34	3De 9	3Po11	7	5	1.033	12.002	118.37	1000.86	1.03E−01	2.45E−03	9.02E+14	8.30E−01
35	34	3Pe 9	3Po11	5	5	1.033	12.002	118.40	1000.86	4.68E−02	7.96E−04	2.93E+14	3.78E−01
35	34	3De 9	3Po11	3	5	1.037	11.956	121.85	1000.86	8.62E−02	8.82E−04	3.21E+14	6.95E−01
35	34	3De 9	3Po11	5	5	1.037	11.956	121.86	1000.86	5.13E−02	8.76E−04	3.19E+14	4.14E−01
35	34	3Pe 9	3Po11	3	5	1.037	11.956	121.87	1000.86	2.63E−07	2.69E−09	9.79E+08	2.12E−06
35	34	1Pe 9	1Po11	3	3	1.033	12.002	118.43	1000.87	6.76E−03	6.89E−05	4.23E+13	5.45E−02
35	34	1De 9	1Po11	5	3	1.033	12.002	118.43	1000.87	5.86E−05	9.97E−07	6.11E+11	4.73E−04
35	34	1Se 9	1Po11	1	3	1.033	12.002	118.44	1000.87	9.76E−02	3.32E−04	2.04E+14	7.87E−01
35	34	3Se 9	3Po11	3	1	1.033	12.002	118.37	1000.89	1.28E−03	1.31E−05	2.41E+13	1.04E−02
35	34	3De 9	3Po11	3	1	1.037	11.956	121.85	1000.89	8.00E−07	8.19E−09	1.49E+10	6.45E−06
35	34	3Pe 9	3Po11	3	1	1.037	11.956	121.87	1000.89	3.44E−02	3.52E−04	6.40E+14	2.77E−01
35	34	3Se 9	3Po11	3	3	1.033	12.002	118.37	1000.90	8.83E−03	9.00E−05	5.52E+13	7.12E−02
35	34	3Pe 9	3Po11	5	3	1.033	12.002	118.40	1000.90	1.83E−03	3.10E−05	1.90E+13	1.47E−02
35	34	3De 9	3Po11	3	3	1.037	11.956	121.85	1000.90	8.91E−04	9.12E−06	5.53E+12	7.19E−03
35	34	3De 9	3Po11	5	3	1.037	11.956	121.86	1000.90	3.16E−03	5.39E−05	3.27E+13	2.55E−02
35	34	3Pe 9	3Po11	3	3	1.037	11.956	121.87	1000.90	6.49E−02	6.64E−04	4.03E+14	5.23E−01
35	34	3Pe 9	3Po11	1	3	1.037	11.956	121.93	1000.90	9.78E−02	3.34E−04	2.02E+14	7.89E−01
35	34	1Pe 9	3Po11	3	5	1.033	12.002	118.43	1000.86	3.65E−04	3.72E−06	1.37E+12	2.94E−03

(*Continued*)

TABLE 9.1 (*Continued*)

Transition Parameters f_{ij}, S, A_{ji}, Cross Section σ_{PI}, and Absorption Coefficient κ for Resonant 1*s*-2*p*, 1*s*-3*p*, and 1*s*-4*p* Transitions in Unfilled *np* Subshells of Bromine II (Ground: $1s^22s^22p^63s^23p^63d^{10}4s^24p^4$). LS Multiplets Are from the Same Spin-Multiplicity Transitions

Z	Ne	slpc:i	slpc:j	g_i	g_j	wl (Å)	E (keV)	E_i (Ry)	E_j (Ry)	f_{ij}	S	A_{ji} ($s-1$)	σ_{PI} (Mb)
						$C_i(9) = 1s^22s^22p^5 \ldots 4p^5$, $C_j(11) = 1s2s^22p^6 \ldots 4p^5$							
35	34	1De 9	3Po11	5	5	1.033	12.002	118.43	1000.86	4.91E–03	8.35E–05	3.07E+13	3.96E–02
35	34	3Se 9	1Po11	3	3	1.033	12.002	118.37	1000.87	7.63E–02	7.78E–04	4.77E+14	6.15E–01
35	34	3Pe 9	1Po11	5	3	1.033	12.002	118.40	1000.87	5.44E–02	9.24E–04	5.67E+14	4.38E–01
35	34	3De 9	1Po11	3	3	1.037	11.956	121.85	1000.87	1.61E–02	1.65E–04	1.00E+14	1.30E–01
35	34	3De 9	1Po11	5	3	1.037	11.956	121.86	1000.87	4.87E–02	8.31E–04	5.03E+14	3.92E–01
35	34	3Pe 9	1Po11	3	3	1.037	11.956	121.87	1000.87	3.89E–03	3.98E–05	2.41E+13	3.14E–02
35	34	3Pe 9	1Po11	1	3	1.037	11.956	121.93	1000.87	5.39E–03	1.84E–05	1.12E+13	4.35E–02
35	34	1Pe 9	3Po11	3	1	1.033	12.002	118.43	1000.89	6.74E–02	6.87E–04	1.26E+15	5.43E–01
35	34	1Pe 9	3Po11	3	3	1.033	12.002	118.43	1000.90	2.85E–02	2.91E–04	1.78E+14	2.30E–01
35	34	1De 9	3Po11	5	3	1.033	12.002	118.43	1000.90	9.80E–02	1.67E–03	1.02E+15	7.91E–01
35	34	1Se 9	3Po11	1	3	1.033	12.002	118.44	1000.90	5.38E–03	1.83E–05	1.12E+13	4.34E–02
LS						880.91	11.985	119.97	1000.87	6.97E–01	7.12E–03	1.45E+15	5.62E+00
Total number of trans = 30						E(keV) = 11.985		f, σ_{PI}, κ =			1.03E+00	8.31E+00	6.26E+04
						$C_i(7) = 1s^22s^22p^63s^23p^5 \ldots 4p^5$, $C_j(11) = 1s2s^22p^6 \ldots 4p^5$							
LS						986.38	13.420	14.49	1000.87	1.44E–02	6.56E–04	1.87E+14	1.16E–01
Total number of trans = 30						E(keV) = 13.420		f, CS, Absrp cf =			8.00E–02	6.45E–01	4.86E+03
						$C_i(1) = 1s^22s^22p^63s^23p^6 \ldots 4p^4$, $C_j(11) = 1s2s^22p^6 \ldots 4p^5$							
LS						1000.83	13.617	0.04	1000.88	2.54E–05	6.85E–07	2.04E+11	2.05E–04
Total number of trans = 14						E(keV) = 13.617		f, CS, Absrp cf =			1.34E–04	1.08E–03	8.13E+00

TABLE 9.2
Averaged Energies E_{res} and Resonant Photoionization Cross Sections σ_{res} for K_α (1s-2p) Transitions in Gold Ions, from Hydrogen-Like to Fluorine-Like

Ion Core	Transition Array	No. of Transitions	$\langle E(K_\alpha)\rangle$ (keV)	$\langle \sigma_{res}(K_\alpha)\rangle$ (Mb)
F-like	$1s^22s^22p^5 \ldots 1s2s^22p^6$	2	68.324	0.99
O-like	$1s^22s^22p^5 \ldots 1s2s^22p^6$	14	68.713	4.10
N-like	$1s^22s^22p^5 \ldots 1s2s^22p^6$	35	68.943	5.17
C-like	$1s^22s^22p^5 \ldots 1s2s^22p^6$	35	69.136	8.63
B-like	$1s^22s^22p^5 \ldots 1s2s^22p^6$	14	68.938	3.48
Be-like	$1s^22s^2 \ldots 1s2s^22p$	2	68.889	3.47
Li-like	$1s^22s \ldots 1s2s2p$	6	68.893	2.82
He-like	$1s^2 \ldots 1s2p$	2	68.703	3.93
H-like	$1s \ldots 2p$	2	69.663	1.58

Source: Pradhan, A. K., S. N. Nahar, M. Montenegro, Y. Yu, H. L. Hang, C. Sur, M. Mrozik, and R. M. Pitzer. 2009. *J Phys Chem A* 113:12356–63. With permission.

We also present similar transition rates for $1s$-$2p$ transitions in gold ions ($Z = 79$, $M = 196.97$ a.u.), from hydrogen-like to fluorine-like ions, in Table 9.2 (Nahar, Pradhan, and Sur 2008; Pradhan et al. 2009). These highly charged ions illustrate all possible transitions among the levels with all possible vacancies in K- and L-shells. We consider the energy region from K-shell excitations up to the K-edge. This refers to the transitions $K \rightarrow L, M, N, O, P, \ldots$ or ΔE ($n = 1 \rightarrow 2, 3, 4, 5, \ldots$), and up to the $1s$ or K-shell ionization energy. The set of resonant K-shell transitions then refers to K_α, K_β, K_γ, K_δ, K_ε, etc. They represent the strongest resonances, and the level of accuracy in the SUPERSTRUCTURE calculations is sufficient for demonstrating the efficacy of monochromatic radiation absorption via these resonances. These yield cross sections that are orders of magnitude larger than that of the background, as shown in Section 9.6. Transition strengths are computed for all possible transitions among fine structure levels SLJ of the K- and L-shells. The number of transitions varies widely for each ion from the H-like to F-like state.

Line or resonance absorption strengths of these ions were used to incorporate broadening profiles for K_α resonances. We computed the resonant photoabsorption cross sections, according to Seaton et al. (1994), as follows:

$$\sigma(K\text{–}L_i) = [4\pi^2 \alpha a_0^2 E(K\text{–}L_i)]/(3g_K)\, S(K\text{–}L_i)\varphi(\nu)$$

where L_i refers to the upper level in the open (ionized) L-shell, $E(K\text{–}L_i)$ is the corresponding energy, $S(K\text{–}L_i)$ is the line strength, and $g_K = 1$ is the initial level statistical weight. The profile factor $\varphi(\nu)$ depends on the plasma temperature and density and is normalized to unity for each resonance complex, K_α, K_β, K_γ, etc., as follows:

$$\int_{\Delta\nu res} \varphi(\upsilon)d\nu = 1$$

Table 9.2 presents the transition arrays, number of resonances N_T, the average K_α energy $E(K_\alpha)$, and cross section $\langle\sigma_{res}\rangle$. $\langle\sigma_{res}\rangle$ was obtained from the total $\Sigma_i\sigma(K\text{–}L_i,E)$ cross section averaged over the K_α energy range $\Delta E_{K\alpha}$ (given by Nahar, Pradhan, and Sur 2008). Each transition corresponds to a specific K_α resonance. Table 9.2 gives a rough estimate of the magnitude of the averaged absorption for each ion. These resonance strengths at energies below the *K*-shell ionization threshold contribute photoabsorption, as discussed in Section 9.6.

9.6 PHOTOABSORPTION COEFFICIENTS OF BROMINE AND GOLD

We study X-ray spectroscopy of BUdR through that of bromine as the active element in the compound. As shown in Table 9.1, bromine emits or absorbs X-rays in the narrow energy range of ~12–14 keV in the (1*s*-*np*) core transitions. The background photoionization, without autoionizing resonances, typically decreases with increase in energy. However, as the energy reaches an inner-shell ionization threshold, the background cross section jumps, but again falls beyond the ionization edge. Figure 9.3 shows background (the curve showing *K*- and *L*-edges) photoabsorption coefficient κ, which is the photoionization cross sections per gram of bromine (NIST). Edges in κ correspond to ionization jumps at various *K*, *L*, *M* (sub)shell energies, with the *K*-shell ionization edge at about 13.5 keV.

Enhanced ionization implies enhanced emission of Auger electrons. Earlier studies have focused on X-ray absorption for ionization at energies of the *K*-shell ionization threshold, and just above, where the cross sections rise over the background. Figure 9.3 shows that although there is a *K*-edge jump, the magnitude is much smaller, by orders of magnitude, than the cross sections at lower energies corresponding to higher shell thresholds. This is the main reason for the low probability of any observable enhancement of emission of electrons. On the other hand, the autoionizing resonances due to 1*s*-*np* transitions lying below the *K*-shell ionization threshold form high-peak resonances (sharp lines), where absorption cross sections are orders of magnitude higher than that at the *K*-shell ionization edge.

Auger processes induced by ionization of the inner-most *K*-shell in bromine, in the radiosensitizing agent BUdR, are not sufficiently strong. They do not lead to significant enhancement in the emission of electrons and photons to break up DNA strands in malignant cells (Larson et al. 1989). But now we invoke the RT mechanism activated via these resonances below the *K*-shell ionization threshold, particularly at energies for the K_α(1*s*-2*p*) transitions in heavier elements such as gold. We assume that *K*-shell ionization can lead to vacancies in higher electronic shells due to the Auger process. Thus, an incident monoenergetic K_α beam of X-rays with sufficient intensity may affect the inverse process, that is, excite the *K*-shell electrons into the *L*-shell. Similarly, monochromatic excitation into higher shells may also be possible through resonant transitions K_β(1*s*-3*p*), K_γ(1*s*-4*p*), etc.

The calculation of averaged plasma attenuation coefficients requires photoabsorption cross sections as a function of incident photon energy. Using the transition rates for the K_α resonances calculated by Nahar, Pradhan, and Sur (2008), we computed

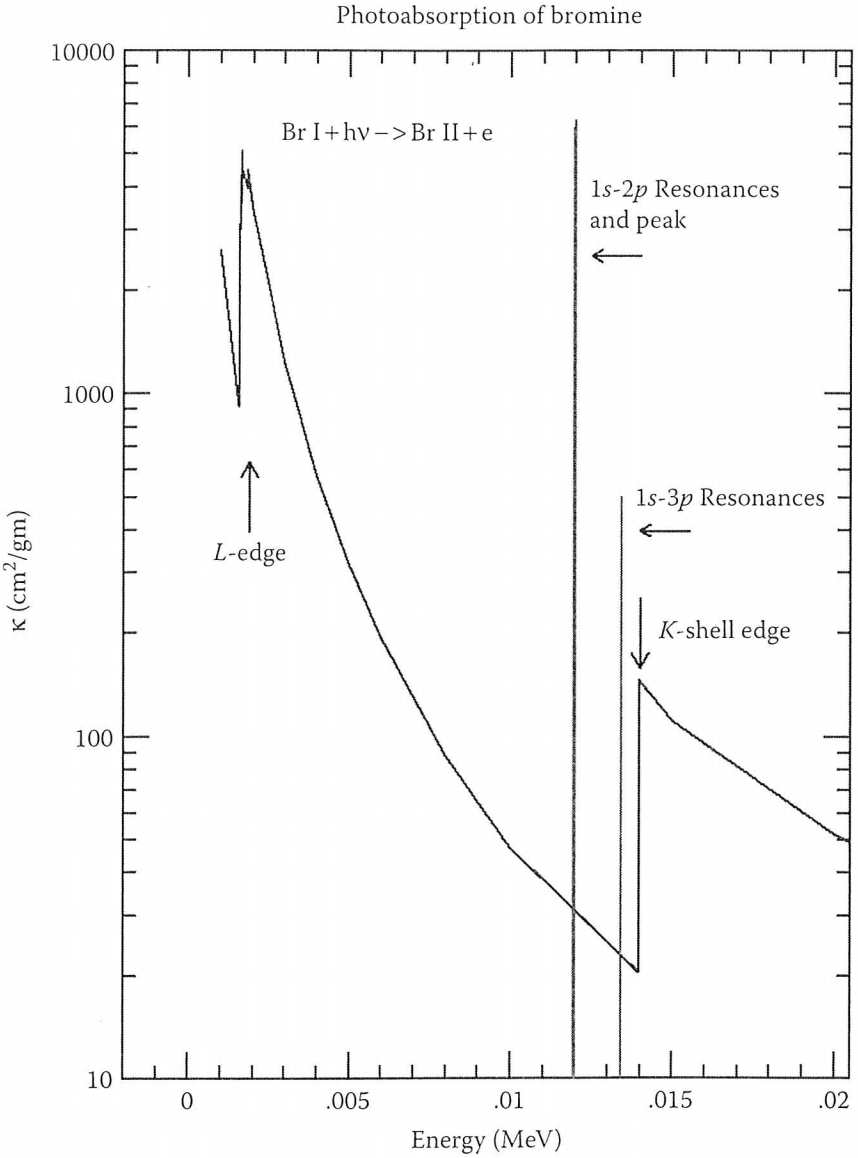

FIGURE 9.3 Photoabsorption attenuation coefficient κ of neutral bromine illustrating resonance effects. The curve is the background cross sections (without resonances) (data from NIST website http://www.nist.gov), where the rise in κ at various energies correspond to ionization edges of the *K* and *L* (sub)shells. The sharp lines correspond to energies and resonance peaks due to 1*s*-2*p* and 1*s*-3*p*, 1*s*-4*p* transitions (3*p* and 4*p* lie together). (From Nahar, S. N., Y. Luo, I. Le, A. K. Pradhan, E. Chowdhury, and R. Pitzer. 2010. In WF06, *Abstracts of 65th International Symposium on Molecular Spectroscopy*, Columbus, OH, June 21–25, p. 197. With permission.)

the resonant photoabsorption cross sections, broadened with an assumed beam width and other broadening effects in the target. Similar convolution was carried out for all individual transitions within higher complexes, such as K_β, K_γ, K_δ, and K_ε, corresponding to transitions to the *M*, *N*, *O*, and *P* shells, respectively. We adopted a normalized Gaussian function φ with an arbitrary full width half maximum (FWHM) of 100 eV, and computed resonant and nonresonant mass attenuation coefficients κ for different gold ions (Pradhan et al. 2009). These mass absorption coefficients are

plotted in Figure 9.4. The background photoionization cross sections including the K-edge for various ionic states were computed using the relativistic distorted wave approximation (Pradhan et al. 2009).

Figure 9.4 presents the monochromatic photoabsorption coefficients of gold ions below the K-edge, 80.729 keV. The ionization stages in various panels correspond to highly ionized L-shell states, from hydrogen- to fluorine-like, that is,

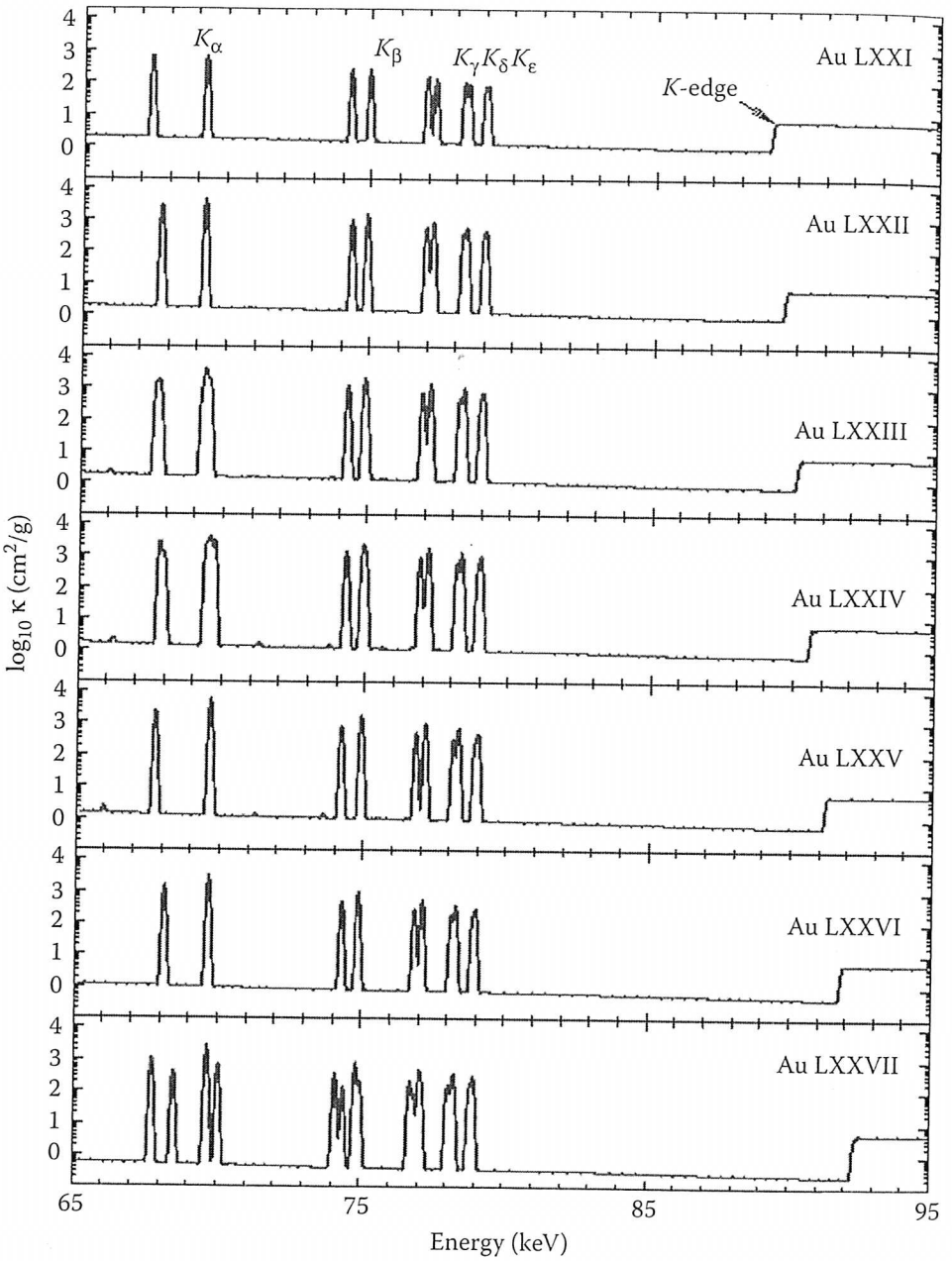

FIGURE 9.4 Total mass attenuation coefficients κ (cm^2/g) for gold ions from Au LXXVII (hydrogen-like) to Au LXXI (fluorine-like). X-rays in the range 67–79 keV are absorbed in the high-peak resonances below the K-shell ionization threshold. The resonance peaks due to $1s$-np transitions in the core (Table 9.2) are orders of magnitude higher than at the K-edge jumps. (From Pradhan, A. K., S. N. Nahar, M. Montenegro, Y. Yu, H. L. Hang, C. Sur, M. Mrozik, and R. M. Pitzer. 2009. *J Phys Chem A* 113:12356–63. With permission.)

ions isoelectronic with H, He, Li, Be, B, C, N, O, and F-like sequences. More enhanced X-ray photoabsorption occurs via a multitude of strong dipole transition arrays (1*s*-*np*). The *K*-shell resonance complexes are found to enhance total absorption by large factors up to 1000 at the corresponding energies relative to the background. In all panels in Figure 9.4, it can be seen that the effects of *K*-shell absorption in all ions, in much of the energy region from the K_α resonance complex up to the *K*-edge (68.7–80.7 keV), could cause considerable X-ray extinction. The total absorption by complexes K_β, K_γ, K_δ, etc., decreases as n^{-3}. However, it may be noted (and not explored before) that these resonant cross sections are orders of magnitude higher than that of the *K*-ionization. Thus, compared to resonant energies, continuum X-ray opacity in the high-energy regime is considerably smaller.

The above findings can be applied to neutral gold. When the *K*-shell is ionized to create one- or two-electron vacancies in the *L*-shell by an external source, then the absorption coefficient for K_α resonant excitation can be taken to be the same as for F-like and O-like gold ions, respectively (Table 9.1). The reason for the approximation is that transition strengths for deep inner-shell transitions, especially the $K \rightarrow L$, are largely unaffected by outer-shell electron correlations and influenced mainly by nuclear charge screening. The total K_α oscillator strengths are approximately independent of *Z* along a given isoelectronic sequence.

Since there is a strong dependence of $\kappa(\nu)$ on each ionization stage capable of *K*-shell excitation, the attenuation coefficient can be written as follows:

$$\kappa(\nu, K_\alpha) = \frac{1}{uW_A} \frac{\sum_j w_j \sum_i \sigma_{res}(\nu, K \rightarrow L_{ji})}{\sum_j w_j}$$

where w_j is the ionization fraction for an ion core *j* in the *L*-shell. For instance, we may perform simulations of X-ray propagation assuming equipartition between only one and two *L*-shell vacancies, that is, excitation of a plasma ionized up to F-like and O-like ions of gold.

It may also be noted that the resonant absorption peaks for gold ions are significantly higher than those of bromine due to the large difference between the nuclear charge of gold and bromine. Gold has higher *Z*, 79, than that of bromine ($Z = 35$), and hence the background cross sections, which show $1/Z^2$ dependence, are lower for gold than bromine. But the oscillator strengths do not depend on *Z* and are of the same order for both elements. Hence, the background-to-resonant peak ratio of gold is much larger than that of bromine.

9.7 TEST OF RESONANT THERANOSTICS USING NUMERICAL SIMULATIONS

Radiation propagation in a medium involves several other processes in addition to those mentioned above. One is "Compton scattering" where the photon transfers some energy to an electron.

$$h\nu + X^{+Z} \leftrightarrow X^{+Z*} + h\nu'$$

This process could be significant for light elements in the body, given high-energy X-ray irradiation. In addition, there are secondary electron collision processes that could be as follows:

1. Ionization: $e + X^{+Z} \rightarrow e' + e'' + X^{+Z+1}$
2. Excitation: $e + X^{+Z} \rightarrow e' + X^{+Z*}$

Hence, in a numerical simulation, these processes need to be considered. We now seek to model the physical processes due to irradiation of X-rays and passage through body tissue interspersed with layers of high-Z material. Our aim is to study the enhanced X-ray interactions owing to the presence of high-Z material and at resonant energies as opposed to the nonresonant background. Modeling of photon transport in biological tissue numerically with Monte Carlo simulations is common and can provide accurate predictions compared to handling a difficult radiation transfer equation or diffusion theory. Monte Carlo simulations can keep track of many physical quantities simultaneously, with any desired spatial and temporal resolution, making it a powerful tool. The simulations can also be made accurate by increasing the number of photons traced. Hence, these methods are standard for simulated measurements of photon transport for many biomedical applications.

Although flexible, Monte Carlo modeling is rigorous since it is statistical and therefore requires significant computation time to achieve precision. In this method, transportation of photons is expressed by probability distributions, which describe the step size of the photon propagation between sites of photon–tissue interaction and the angles of deflection in the photon's trajectory when a scattering event occurs. The required parameters needed are the absorption coefficient, the scattering coefficient, the scattering phase function, and so on. As the photon interacts with the medium, it deposits energies due to absorption and is scattered to other parts of the medium. Any number of variables can be incorporated along the way, depending on the interest of a particular application. Each photon packet will repeatedly undergo a number of steps until it is terminated, reflected, or transmitted.

Compared to other simulations for biological systems, relatively fewer codes are capable of describing effects of radiation in microscopical entities, such as cellular structures and the DNA molecule, of size of the order of a few nanometers or tens of nanometers. However, few general Monte Carlo codes have the capability of describing particle interactions at these scales. The Monte Carlo simulation code Geant4 (Agostinelli et al. 2003) is enough to consider the radiation transport and high-energy X-rays needed to model RT. It is an open-source code developed with an object-oriented design with the possibility to implement or modify any physical process without changing other parts of the code. Its versatility has enabled its application to medical physics.

9.7.1 Monte Carlo Simulations Using Geant4

We have adopted the Monte Carlo code Geant4 version 9.2 for the simulations of X-ray absorption by gold nanoparticles at resonant energies (Montenegro et al. 2009). The physical phenomena were not heretofore explored. The Geant4 package

treats atoms as neutral, and photoelectric cross sections do not include electronic shell-ionization effects. We have modified the code such that it can include the resonant cross sections in addition to its own input data for various processes. Geant4 has an extension package known as "low-energy electromagnetic processes," which is the product of a wider project called Geant4-DNA, which addresses specifically the extension of Geant4 to simulate radiation effects at the cellular and DNA scales, and has been widely tested. It includes the Auger process. It is this package that has been modified to consider resonant enhancement and fluorescent yields that may be used for monochromatic imaging and diagnostics, as well as therapy. However, the standard version of Geant4 we have modified to accommodate resonant structures does not include shell structures in an atomic system and hence is incapable of treating the Coster–Kronig cascade process.

For numerical simulations, we perform a test for a tumor measuring $2 \times 5 \times 5$ cm^3 located 10 cm below the skin and assume that it is doped with a thin layer of gold nanoparticles. Since the muscular tissue has a density of 1.06 g/mL similar to that of water (1.0 g/mL), the numerical experiments were carried out in a phantom of water $15 \times 5 \times 5$ cm^3 with a thin layer of gold nanoparticles of 2-cm thickness with 0.1 mm/g at 10 cm inside from the surface. The phantom setup is shown in Figure 9.5a. Monochromatic X-rays of various energies are passed separately through the water into the thin layer of gold nanoparticles.

We assumed preionization of gold atoms by another X-ray beam at energy above the *K*-edge energy of ~81 keV to create electron vacancies (as illustrated in Figure 9.2). The simulations considered resonances for the preionized atomic core of gold ions Au LXXI (or F-like with one-electron vacancy) and Au LXXII (or O-like with two-electron vacancies). We assume equipartition between these two ion cores for simplification of the calculation of the resonant cross sections and reduced the cross sections to be just the average value of both ions, for example, an estimate of

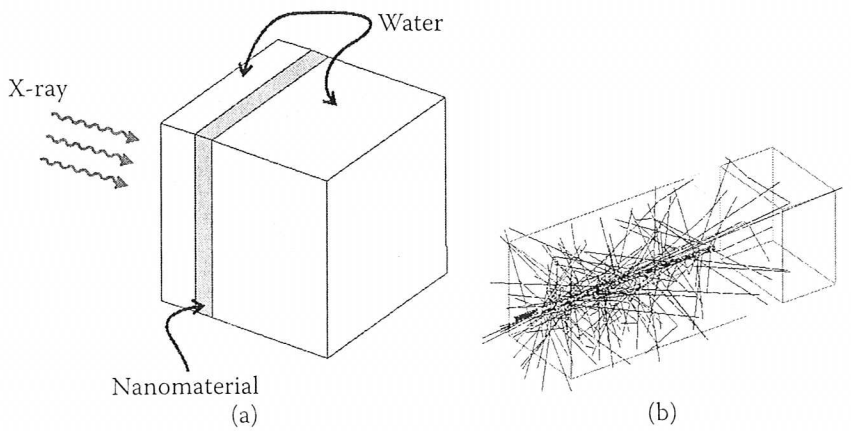

FIGURE 9.5 (a) Geometry of the Geant4 simulations. The water phantom models a tumor (nanomaterial) 10 cm inside normal tissue. The monochromatic beam collides perpendicular to the square face of the water block. (b) Snapshot of 68-keV X-ray photons propagating inside the tissue. Black lines show the photon trajectories in the phantom. The tumor is embedded with gold nanoparticles at 5 mg. Note how only a small fraction of photons are able to cross the region up to the gold nanoparticles.

~2.5 megabarns (1 MB = 10^{-18} cm^2) at ~68 keV. Outside the resonant energies of these ions, the gold nanoparticles were assumed neutral.

To see the resonant effect, we passed three different monochromatic X-rays into the phantom: (1) a beam with a beam energy corresponding to the averaged K_α energy at 68 keV, which is the energy difference between the L ($n = 2$) and the K ($n = 1$) shells, (2) an 82-keV beam, with energy just above the ionization energy of the K-shell electrons at 81 KeV, and (3) a high-energy beam of 2 MeV, which corresponds to the maximum intensity of the Bremsstrahlung radiation distribution from a LINAC with 6-MVp peak voltage X-ray source used in many medical facilities. A "snapshot" of the propagating beam at 68 keV is shown in Figure 9.5b. It shows that there are strong photon interactions being deflected or absorbed, reducing drastically the number of available photons to reach the tumor or beyond.

9.7.2 Resonant Effects on Monte Carlo Simulations

The X-ray irradiation of gold ions results in Auger decays of photon emission and electron ejections, creating multiple electron vacancies. These vacancies may be filled either by radiative decays from higher electron shells or by excitations from the K-shell at resonant energies by an external X-ray source. One main objective was to observe the predicted enhancement in absorption of X-rays at 68 keV resonant energy by gold nanoparticles as this would provide a new insight into unsuccessful experimental searches to find such enhancement at and around the K-shell ionization energy of ~81 keV. The absorption spectra from the Monte Carlo simulations on extinction of X-rays with depth from the surface are shown in Figure 9.6. The darker curves represent absorption by the body muscle without the nanoparticles and the lighter curves that with the nanoparticles. The incident X-ray energies are high for any resonance for the water molecules. Hence, these molecules experience only Compton scattering with small cross sections and produce some low-energy electrons. The rise in the lighter curves at the entrance of the tumor, 10 cm inside, in each panel shows the energy deposited in the nanoparticles. Figure 9.6 shows that resonant excitations via K_α, K_β, etc., transitions result in a considerable enhancement in localized X-ray energy deposition at the layer with nanoparticles compared with nonresonant processes and energies. The top panel shows that the absorption peak at 68 keV is considerably higher, ~10.6 keV/mm, compared to the nonresonant background and complete absorption of radiation within the layer.

The enhanced absorption at 68 keV is expected to lead to enhanced emission of photons and electrons to kill the tumor cells. The peak in the middle panel, ~0.38 keV/mm for 82 keV X-rays, is relatively small, which results in no visible rise in secondary electron production. The lowest panel shows an X-ray absorption peak of ~4 keV/mm for 2 MeV X-rays. This peak is higher, although lower than that of 68 keV, because of higher penetration of the beam into the tissue. Both the 68 keV and the 82 keV X-ray beams in the top and middle panels could retain only about a quarter of their intensity before reaching the tumor, whereas the 2 MeV beam in the bottom panel has little interaction with the tissue, and the deposited energy is reduced by only about 20% before reaching the tumor. This is the primary reason for the use of high-energy beams, to ensure that the tumor receives a sufficiently

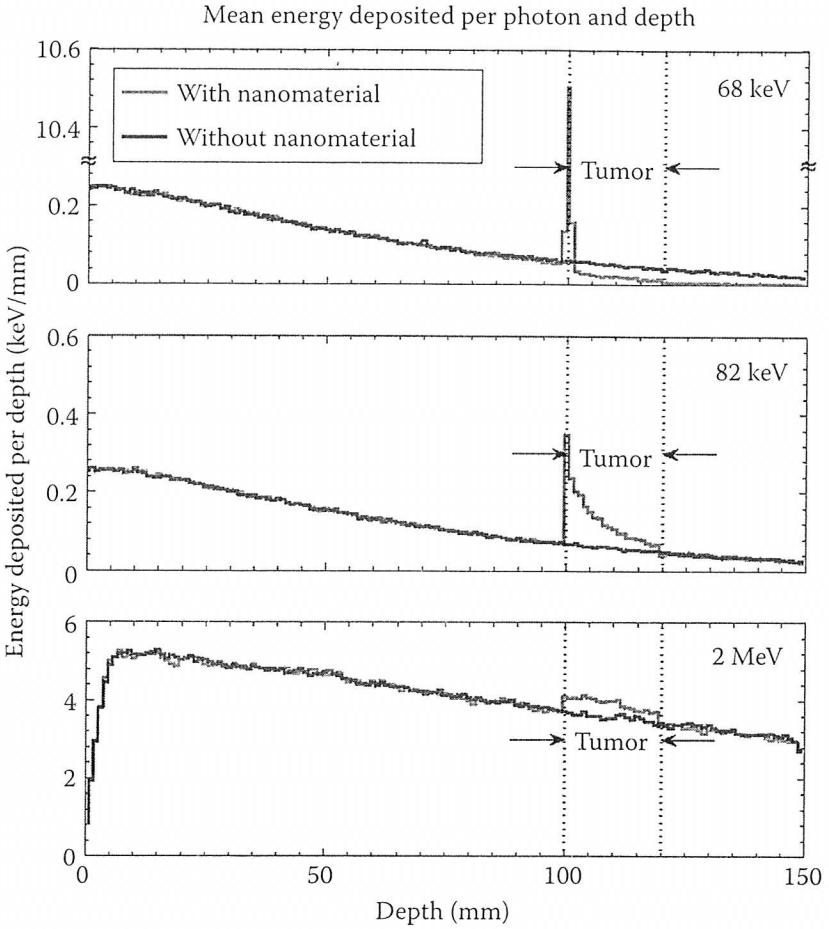

FIGURE 9.6 X-ray energy deposition by depth across the phantom at three X-ray beams used: 68 keV (averaged K_α resonant energy), 82 keV (K-edge energy), and 2 MeV (high energy common in clinical usage). The region between 100 and 120 mm represents the tumor, and it can be embedded with gold nanoparticles at 5 mg/mL (lighter curve) or water (darker curve). The presence of gold nanoparticles increases the energy deposited at the tumor. The highest absorption is at 68 keV, more than 25 times higher than that at 82 keV.

high-radiation dose. The downside of this approach is that not only the tumor but also the normal tissue along the beam path receives high dosage.

The simulations also show that with higher X-ray absorption a larger number of secondary Auger electrons are produced, as illustrated in Figure 9.7. Again, the darker curve represents the water or body tissue, while the lighter curve represents electron production by the water; the gold nanoparticles are assumed to be placed at 10 cm from the surface. While a small rise in electron production is noted for 82 keV and at 2 MeV (middle and the lowest panels), a high peak in the electron counts is seen at the resonant energy of 68 keV, assuming existing L-shell vacancies created by a preionization X-ray beam. A larger number of electrons, by more than an order of magnitude, are then produced at 68 keV compared with that at 82 keV. Consistent with deeper penetration by high-energy X-rays, the high-energy beam at 2 MeV produced more electrons than that at 82 keV, but still much smaller than that at 68 keV.

The photoelectrons produced by the X-ray irradiation should trigger the breakage of DNA strands and, consequently, destruction of cancerous cells. The

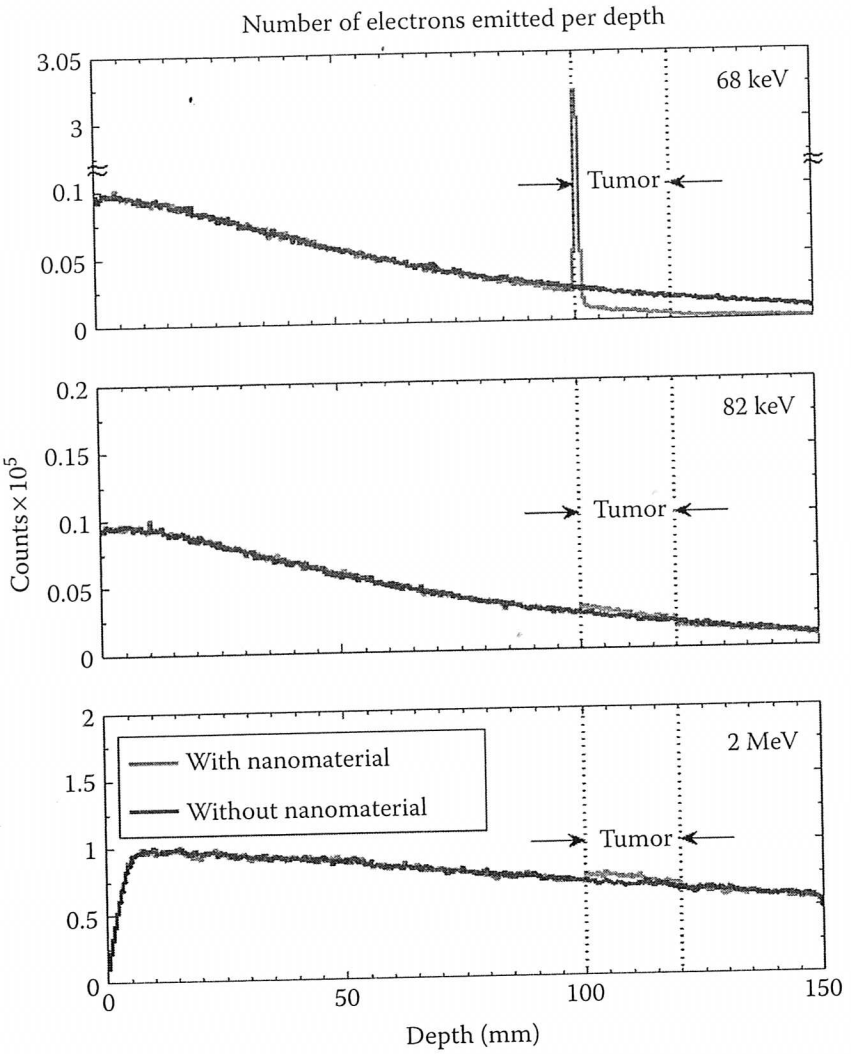

FIGURE 9.7 Electron production with depth at the three X-ray beam energies 68 keV, 82 keV, and 2 MeV. Auger production of electron peaks at 68 keV are higher by more than an order of magnitude than at 82 keV, and over five times that at 2 MeV.

low-energy photoelectrons produced in the tumor are absorbed in the immediate vicinity. The mean free paths of electrons produced from gold nanoparticles are 47, 46, and 52 μm for the 68 keV, 82 keV, and 2 MeV beams, respectively, compared with the 1-mm mean free path of electrons produced in the water portion of the phantom.

In contrast to electron emissions, photon production is relatively low since most of the input energy from the incident X-ray beams goes into the production of Auger electrons and relatively little to secondary photons via fluorescence. Figure 9.8 shows production of photons with depth from the three different X-ray energies. Darker curve represents photon production from water, and the lighter curve represents photon production with gold nanoparticles. The number of photons produced by the 68-keV X-ray beam shows a clear surge at the tumor site, while the production is almost invisible for the 82 keV and 2 MeV beams.

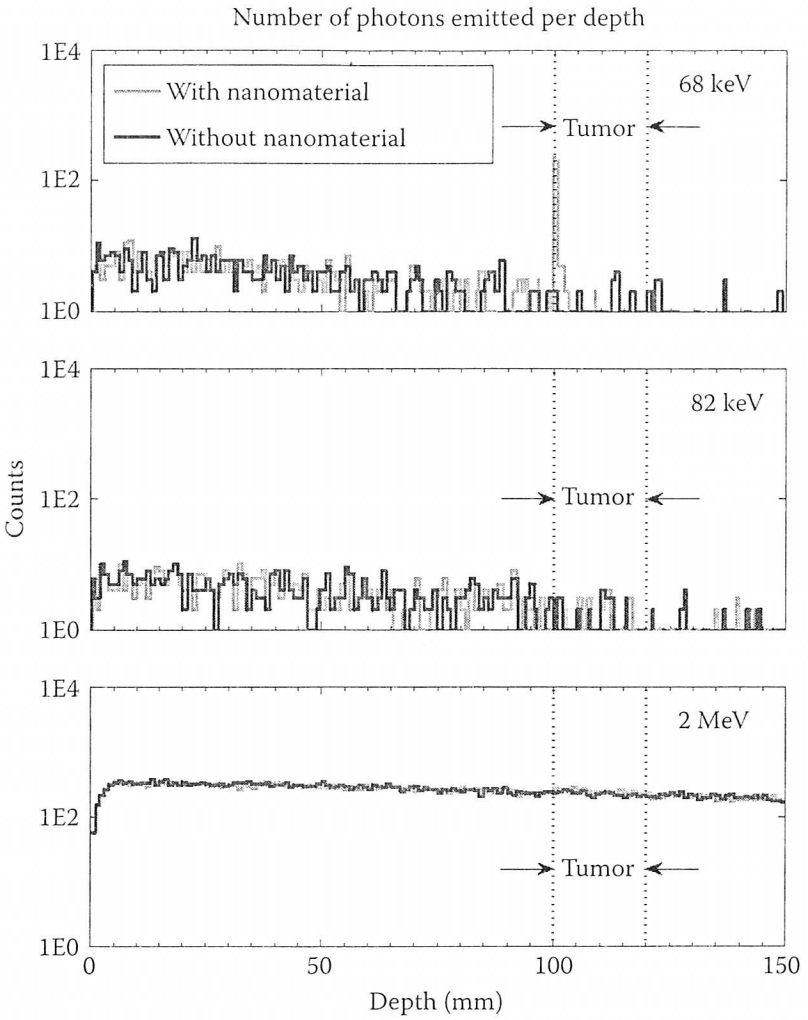

FIGURE 9.8 Photon emission with depth inside the phantom at three X-ray beams: 68 keV, 82 keV, and 2 MeV. Only 68 keV shows a surge in photon production.

9.8 RADIATION DOSE ENHANCEMENT FACTOR

The radiation dose enhancement factor (DEF) is defined as the ratio of the average radiation dose absorbed by the tumor when it is loaded with a contrast medium or agent (e.g., iodine) to the dose absorbed without the agent. We consider the nanoparticle solution as the contrasting medium. These values can be obtained from Figure 9.6 by integrating over the energy absorbed by the tumor with and without nanoparticles, using the same phantom under both conditions. The ratio of the mean total energy absorbed per photon by the tumor under the two conditions gives the DEF.

The simulations also assumed different concentrations of the gold nanoparticles from 0 to 50 mg/mL. DEFs were obtained by irradiation at the three energies: 68 keV, 82 keV, and 2 MeV. The phantom was divided longitudinally into sections of 1 mm, and the energy deposition, as well as particle generation, at each slice was recorded. A monochromatic linear beam, with a circular cross section of 3-mm diameter, was aimed at the phantom perpendicular to the square face far from the tumor region. Each simulation had 500,000 events, a value that generates error fluctuations of less than 0.1%.

The results are plotted in Figure 9.9. The DEFs obtained for the resonant X-ray beam of 68 keV are almost an order of magnitude greater, even at low concentrations, than those calculated at higher energies and concentrations. At 68 keV, the DEF at a concentration of 5 mg/mL was 11.02 and increased slowly to 11.7 for a concentration of 50 mg/mL. This indicates that low concentration is sufficient to achieve high DEF for resonant energies. On the other hand, the DEFs for the 82-keV beam increased steadily from about 1 to achieve the high DEFs obtained in the resonant case. For the 2 MeV case, we obtained low but slowly increasing values of DEFs as the concentration increased, confirming our observation in Figures 9.6 and 9.7. It is possible to obtain an enhanced dosage with high-energy beams. But the enhancement is quite small and increases slowly with nanoparticle concentrations. The behavior shown in these curves is in agreement with the calculations done by Solberg, Iwamoto, and Norman (1992), from which they found that DEF with a 250-keV beam was smaller, and had a weaker concentration dependence, than that with a 140-keV beam.

The almost flat behavior for the DEF at 68 keV can be explained by the large mass attenuation factor obtained, 39.1 cm^2/g for 68 keV versus 0.241 cm^2/g for 82 keV at 5 mg/mL. This high mass attenuation coefficient results in a complete absorption of any incoming photon within the tumor region surface, reducing the transmission probability and any further increase due to subsequent absorption beyond. This saturation of the absorption is also observed at high gold concentrations for the 82-keV beam, asymptotically reaching the same value as the 68-keV beam (extending the results in Figure 9.9 to high, though unrealistic, concentrations).

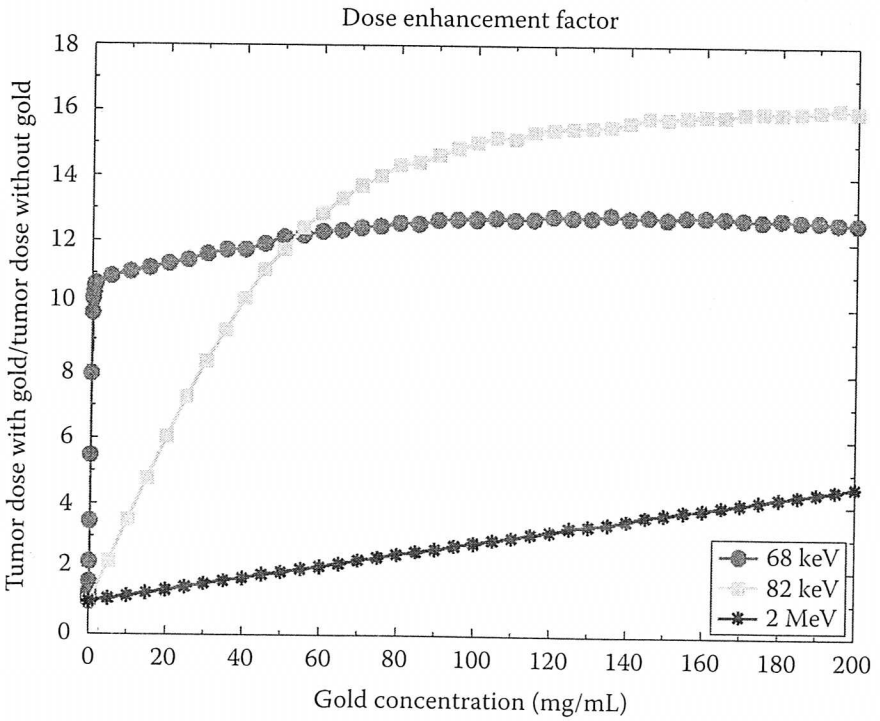

FIGURE 9.9 Dose enhancement factors at three X-ray energy beams, 68 keV, 82 keV, and 2 MeV for different concentration of gold nanoparticles.

9.9 CONCLUSION

The present results based on the RT method could be applicable to in vivo therapy and diagnostics of cancerous tumors using high-Z nanoparticles and monochromatic X-ray. X-ray radiation dose reduction commensurate with resonant enhancements may be realized for cancer theranostics, using high-Z nanoparticles and molecular radiosensitizing agents embedded in malignant tumors. The in situ deposition of X-ray energy, followed by secondary photon and electron emission, should also be localized at the tumor site. We also note the relevance of this work to the development of novel monochromatic or narrow-band X-rays. The underlying mechanism also rests on the biotechnology of high-Z nanoparticles delivered to specific sites, such as cancerous tumors, and then treated with monoenergetic X-rays at resonant atomic and molecular transitions.

Further studies based on the RT method may lead to the use of focused narrow-band or monoenergetic X-ray beams at resonant energies, with a high potential for a much safer treatment of cancerous tumors. However, verification of the absorption enhancement will require collaborative experimental setups with the eventual goal of clinical studies. This multidisciplinary effort involving atomic and molecular physics, chemistry, radiation oncology, nanobiomedicine, and clinical research should lead to advances in the use of narrow-band X-ray using high-Z nanoparticles in biomedical applications.

ACKNOWLEDGMENTS

The work reported herein was partially supported by grants from the Ohio State University and the U.S. National Science Foundation. The computational work was carried out mainly at the Ohio Supercomputer Center in Columbus, Ohio.

REFERENCES

Agostinelli, S. et al. 2003. Physics research section A: Accelerators, spectrometers, detectors and associated equipment. *Nucl Instrum Methods* 506:250–303.

Eissner, W., M. Jones, and H. Nussbaumer. 1974. Techniques for the calculation of atomic structures and radiative data including relativistic corrections. *Comput Phys Commun* 8:270–306.

Hainfeld, J. et al. 2004. The use of gold nanoparticles to enhance radiotherapy in mice. *Phys Med Biol* 49:N309–15.

Larson, D., W. J. Bodell, C. Ling, T. L. Phillips, M. Schell, D. Shrieve, and T. Troxel. 1989. Auger electron contribution to Bromodeoxyuridine cellular radiosensitization. *Int J Radiat Oncol Biol Phys* 16:171–6.

Mass Absorption Coefficients. National Institute of Standards and Technology website: http://physics.nist.gov/PhysRefData/Xcom/Text/download.html.

Monte Carlo Simulation. Palisade Corporation. http://www.palisade.com/risk/monte_carlo_simulation.asp. Accessed July 15, 2011.

Montenegro, M., S. N. Nahar, A. K. Pradhan, Y. Yu, and K. Huang. 2009. Monte Carlo simulations and atomic calculations for Auger processes in biomedical nanotheranostics. *J Phys Chem A* 113:12364–9.

Nahar, S. N. 2006. Atomic data from the iron project - LXI. Radiative E1, E2, E3, and M1 transition probabilities for Fe IV. *Astron Astrophys* 448:779–85.

Nahar, S. N., W. Eissner, G.-X. Chen, and A. K. Pradhan. 2003. Atomic data from the Iron Project - LIII. Relativistic allowed and forbidden transition probabilities for Fe XVII. *Astron Astrophys* 408:789–801.

Nahar, S. N., Y. Luo, I. Le, A. K. Pradhan, E. Chowdhury, and R. Pitzer. 2010. X-ray spectroscopy of bromine compounds and biomedical applications. In WF06, *Abstracts of 65th International Symposium on Molecular Spectroscopy*, Columbus, Ohio, June 21–25, p. 197: http://molspect.chemistry.ohio-state.edu/symposium/abstractbook/absbk10.pdf.

Nahar, S. N., A. K. Pradhan, and C. Sur. 2008. Oscillator strengths and radiative transition rates for Kα lines in gold X-ray spectra: 1*s*-2*p* transitions. *J Quant Spec Rad Transf* 109:1951–9.

Nahar, S. N., A. K. Pradhan, and S. Lim. 2011. Kα transition probabilities for platinum and uranium ions for possible X-ray biomedical applications. *Can J Phys* 89:483–494.

NIST handbook. http://www.nist.gov/physlab/data/handbook/index2.cfm.

Pradhan, A. K., and S. N. Nahar. 2011. *Atomic Astrophysics and Spectroscopy*. Cambridge University Press (Cambridge, UK).

Pradhan, A. K., S. N. Nahar, M. Montenegro, Y. Yu, H. L. Hang, C. Sur, M. Mrozik, and R. M. Pitzer. 2009. Resonant X-ray enhancement of the Auger effect in high-Z atoms, molecules, and nanoparticles: Biomedical applications. *J Phys Chem A* 113:12356–63.

Pradhan, A. K., Y. Yu, S. N. Nahar, E. Silver, and R. Pitzer. 2007. Computational methodology for resonant nano-plasma theranostics for cancer treatment. In *Proceedings of 15th International Conference on the Use of Computers in Radiation Therapy*, Toronto, Ontario, Canada, June 4–7, 2007. http://www.iccr2007.org/.

Seaton, M. J., Y. Yan, D. Mihalas, and A. K. Pradhan. 1994. Opacities for stellar envelopes. *Mon Not R Astron Soc* 266:805–28.

Silver, E., A. K. Pradhan, and Y. Yu. 2008. The X-ray reloaded: Rearming radiography with resonant theranostics. *RT Image* 21:30–4.

Solberg, T. D., K. S. Iwamoto, and A. Norman. 1992. Calculation of radiation dose enhancement factor for dose enhancement therapy of brain tumors. *Phys Med Biol* 37:439–43.